Article

Not peer-reviewed version

Fault Geometry and Tectonic Implications of the 2019 Mw=5.8 Mirpur Earthquake Sequence, Pakistan

Mohammad Tahir , Muhammad Zafar Iqbal , Muhammad Naveed Mushtaq , Aftab Alam , Raja Adnan , Kyriaki Kiskira , Christos Drosos , Georgios Priniotakis , Talat Iqbal , Muhammad Rafique , Dimitrios Nikolopoulos *

Posted Date: 18 March 2026

doi: 10.20944/preprints202603.1351.v1

Keywords: moment tensor inversion; present-day stress condition; seismo-tectonic modeling; Samwal and Pabbi anticline

 doi:10.20944/preprints202603.1351.v1

Article

Fault Geometry and Tectonic Implications of the 2019 Mw=5.8 Mirpur Earthquake Sequence, Pakistan

Mohammad Tahir [1], Muhammad Zafar Iqbal [1], Muhammad Naveed Mushtaq [1], Aftab Alam [1], Raja Adnan [1], Kyriaki Kiskira [2], Christos Drosos [2], Georgios Priniotakis [2], Talat Iqbal [1], Muhammad Rafique [3] and Dimitrios Nikolopoulos [2,*]

[1] Centre for Earthquake Studies (CES), National Centre for Physics (NCP), Islamabad, Pakistan

[2] Department of Industrial Design and Production Engineering, University of West Attica, Petrou Ralli & Thivon 250, GR 122 44, Aigaleo, Greece

[3] Department of Physics King Abdullah Campus, University of Azad Jammu and Kashmir Muzaffarabad, Azad Kashmir, Pakistan, Muhammad Rafique

* Correspondence: dniko@uniwa.gr; Tel.: +302105381338

Abstract

The tectonic framework of the 2019 Mirpur seismic sequence was investigated using local seismic data. Moment tensor inversion was performed for the Mirpur mainshock (Mw=5.8) and its largest aftershock (Mw=4.7). The mainshock exhibited a low dip angle (~10°) and shallow focal depth, suggesting association with the Main Frontal Thrust (MFT). Contrary, the largest aftershock showed a comparatively higher dip angle, indicating deformation along a ramp or ramp-anticline structure. The stress regime was evaluated using moment tensor solutions from two locally inverted events, two Global CMT solutions and a published focal mechanism. The results indicated a maximum horizontal stress (SHmax) orientation of N07°E, consistent with the stress orientation of the 2005 Kashmir earthquake sequence and the regional compression driven by the Indian plate convergence. Aftershock relocation and spatial distribution patterns suggested post-seismic stress relaxation and possible activation of a higher-dip fault segment or ramp-anticline structure. Although a seismogenic depth of approximately 15 km was estimated, the concentration of seismicity around 10 km depth may involve the Main Himalayan Thrust (MHT). The Mirpur mainshock was triggered primarily by the movement along the MFT, whereas the subsequent aftershocks reflected post-seismic relaxation associated with the MHT and related ramp-anticline structures.

Keywords: moment tensor inversion; present-day stress condition; seismo-tectonic modeling; Samwal and Pabbi anticline

1. Introduction

Recent studies indicate an increase in seismic activity in the Mirpur region of northeastern Pakistan, largely highlighted by the Mw=5.9 earthquake of September 24, 2019. This event was the most destructive in the area since 2005, causing 39 fatalities, 746 injuries, and the collapse of nearly 15,000 buildings [1–3]. Owing to its shallow focal depth and proximity to the Mangla reservoir and the Upper Jhelum Canal, the earthquake generated severe secondary hazards, particularly widespread liquefaction and lateral spreading [4,5]. These processes led to extensive ground failure and exposed the high seismic vulnerability of regional infrastructure [6]. The scale of destruction was further intensified by inadequate preparedness measures, the absence of detailed local seismic hazard assessments, and the widespread use of substandard construction materials incapable of resisting lateral seismic forces [4,5,7,8]. Reducing future risk will require improvements in seismotectonic modelling and the integration of high-resolution regional data to better assess earthquake impacts and support effective disaster planning [9–16].

 doi:10.20944/preprints202603.1351.v1

Previous studies have linked the 2019 earthquake in Mirpur to the Main Frontal Thrust (MFT) or one of its associated splay faults, based on seismic and geodetic observations [1,2]. Despite this general association, substantial uncertainty persists regarding the event's source mechanism, centroid location, and focal depth. Importantly, no previous investigations have incorporated waveform inversion using data from local seismic stations, leaving key aspects of the rupture process unresolved. Reported dip angles vary widely, from 5° to 20°, with depth estimates ranging between 5 km and 15 km. Steeper dip solutions tend to support rupture along a splay fault, whereas lower dip-angle models are more consistent with slip along the main MFT surface [1,2,17,18].

These unresolved structural and source-related uncertainties are further underscored by continued seismic activity in the region. A magnitude 5.0 earthquake on 5 December 2024 near Kharian, approximately 30 km south of Mirpur, highlights the ongoing tectonic deformation along the MFT system and reinforces the need to better understand fault geometry, stress transfer, and possible triggering relationships within this structurally complex setting.

To address these issues, this study integrates multiple seismological and tectonic approaches to provide a more robust characterization of faulting and stress evolution in the region. A moment tensor inversion of the 2019 Mirpur earthquake and its largest aftershock was performed using local waveform data from the Centre for Earthquake Studies and Pakistan Meteorological Department seismic networks, thereby improving constraints on source parameters that were previously uncertain. For present-day stress analysis, focal mechanism solutions from the Global CMT catalog and recent regional studies are incorporated. In addition, a comparative neotectonic assessment is conducted with the seismically active Kashmir region, particularly in relation to structural characteristics observed after the 2005 earthquake. Finally, to better understand post-seismic structural reactivation and crustal deformation processes, aftershock relocation and seismogenic depth estimation are performed.

2. Seismotectonics and Geology of the Region

Structurally, the Mirpur region occupies a key position along the southwestern margin of the Himalayan arc, where deformation patterns change markedly across the northwestern orogenic front [19,20]. This zone forms part of a major tectonic bend that links the dominantly compressional central Himalaya with the more complex transpressional regime of the western Himalaya [21,22]. Here, the oblique convergence between the Indian and Eurasian plates—occurring at rates of roughly 5 mm/yr—produces a partitioned deformation field, expressed through southward-directed crustal shortening combined with lateral strike-slip motion [23–28]. The tectonic importance of this region was dramatically demonstrated by the 2005 earthquake in the Kashmir region (Mw=7.7), widely interpreted as an out-of-sequence rupture based on geodetic and interferometric observations [29–33].

Regional shortening in the northwestern Himalaya is accommodated by a series of stacked and imbricated thrust systems that collectively form a well-developed fold-and-thrust belt [34–39] (Figure 1). These major thrusts progressively transfer deformation toward the foreland, with the frontal structures marking the present active boundary of Himalayan tectonics [40–43]. At depth, these surface faults merge into a regional low-angle detachment that facilitates underthrusting of the Indian lithosphere beneath Eurasia [2,44–46]. Superimposed on this compressional framework, lateral deformation is accommodated along major strike-slip structures, including the Jhelum Fault, which trends along the western margin of the arc and plays a key role in redistributing strain around the tectonic bend [47–52]. By enabling lateral extrusion of crustal blocks, this fault helps accommodate variations in convergence direction and contributes to the region's transpressional character [53–55].

Farther south, deformation propagates into the Potwar Plateau and the Salt Range, where a classic thin-skinned fold-and-thrust system has developed above a weak evaporitic detachment horizon. Structural styles in this foreland belt include fault-propagation folds, duplex systems, and triangle zones, all reflecting progressive outward growth of the Himalayan wedge [56–60]. Positioned between the mountain front and the foreland basin, the Mirpur area represents a transitional

 doi:10.20944/preprints202603.1351.v1

structural domain where deep underthrusting, strike-slip partitioning, and thin-skinned shortening interact to produce a highly three-dimensional deformation field [61].

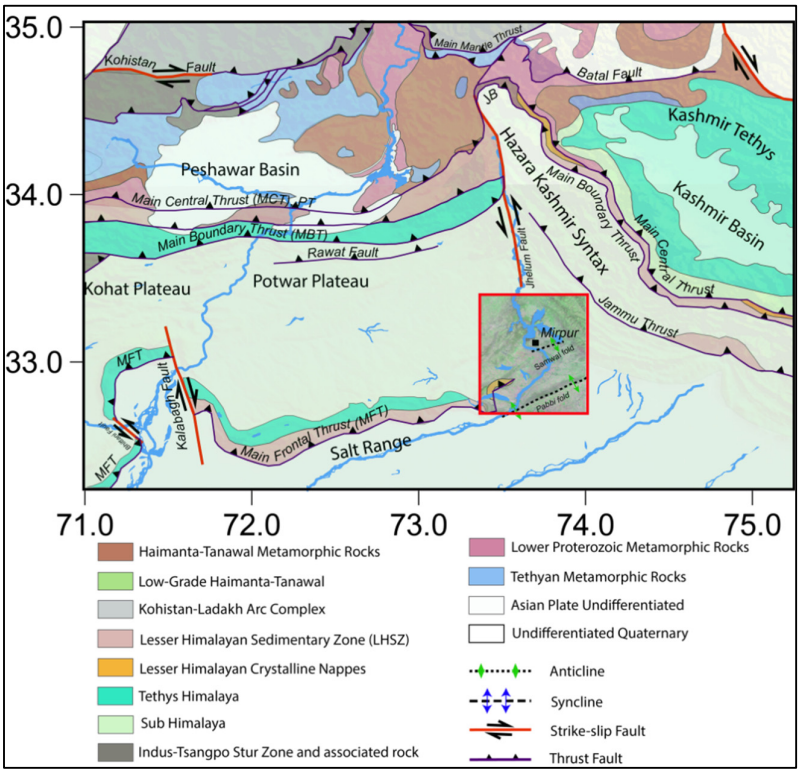

Figure 1. Regional geological and tectonic map of the NW Himalayan foreland fold-and-thrust belt modified from [103–105]. Major thrust systems, fold structures, and tectonic boundaries related to the ongoing convergence between the Indian and Eurasian plates are shown. Prominent tectonic features of the Himalayan foreland belt, including the Main Frontal Thrust and associated fold-and-thrust structures, are indicated to provide the regional tectonic framework. Rectangle shows the study area. Samwal and Pabbi anticline structures acting as blind thrust are shown with dotted lines.

This tectonic complexity is reflected in ongoing seismic activity. The 2019 earthquake south of Mirpur ruptured a shallow thrust structure, interpreted as either a frontal imbricate or a splay related to the active thrust front [1,2,18]. The event occurred near a major fault-propagation fold, and focal-mechanism solutions across the broader region consistently show a mixture of thrust and strike-slip faulting, confirming the influence of transpressional strain associated with arc curvature.

South of Mirpur, the Pabbi Anticline represents another important structural element of the foreland system. Interpreted as a fault-propagation fold above a blind thrust, this structure is thought to have developed during the late Quaternary and has influenced regional drainage evolution, including modification of the Jhelum River [41]. Subsurface data indicate that the fold extends several kilometres in thickness and merges downward into deeper structural levels. Recent seismic activity, including a moderate-magnitude earthquake in December 2024, confirms that this structure remains tectonically active. Consequently, understanding its geometry and evolution is essential for evaluating seismic hazard and reconstructing the ongoing tectonic development of the northwestern Himalayan foreland.

 doi:10.20944/preprints202603.1351.v1

3. Data and Method

3.1. Seismic Data Compilation

Local seismic data from the Centre for Earthquake Studies and the Pakistan Meteorological Department (PMD) were used to perform moment tensor inversion of the 2019 Mirpur earthquake sequence and to investigate its seismotectonic implications. The combined seismic network comprises 49 stations, including 33 operated by CES and 16 by PMD, distributed across different parts of Pakistan (Figure 2). These networks have been operational since 1976, with data transmitted to the central processing facility in Islamabad via radio and satellite links. Most stations are equipped with broadband seismometers and record continuously, ensuring high-quality and consistent waveform acquisition (see [21,30,31,62] for detail).

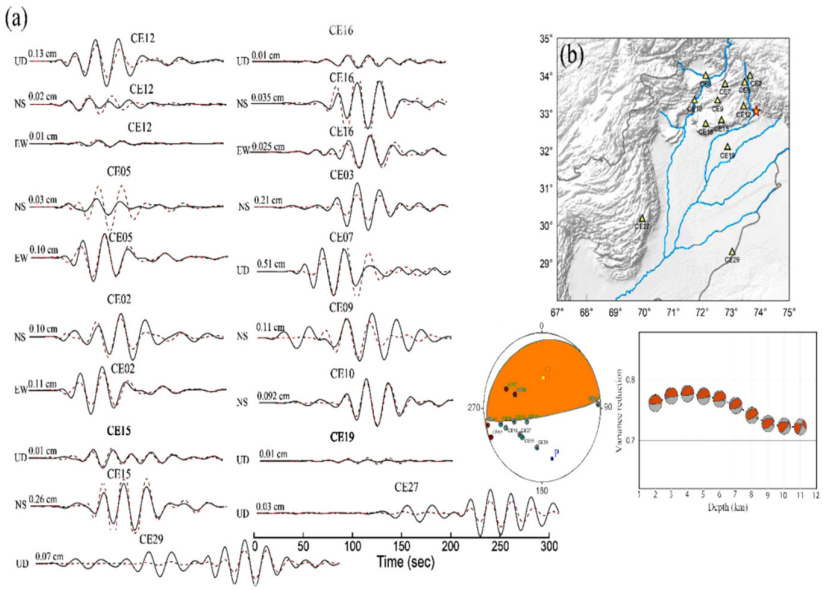

Figure 2. (a) Comparison of observed (solid lines) and synthetic (dotted lines) waveforms for the 2019 Mirpur mainshock. The seismic station code, maximum amplitude, and the corresponding component used in the inversion are indicated at the top and front respectively. The focal mechanism solution (beach ball) with polarity is shown. Variance reduction values at different depths are presented in the lower right corner. (b) Epicentral location of the Mirpur earthquake (star) along with the distribution of seismic stations (triangles) operated by the Centre for Earthquake Studies and the Pakistan Meteorological Department.

Hypocentral parameters, including origin time, focal depth, and epicentral location were determined using the SEISAN software package through the HYPOCENTER location algorithm [63–66]. Events with Round Mean Squares (RMS) residuals less than 0.3 s were regarded as well located [66]. The Centre for Earthquake Studies catalog reports average uncertainties of approximately 8 km in location and 0.2 units in local magnitude (ML) [67–69].

3.2. Waveform Inversion

Waveform inversion was carried out using the ISOLA software package [70,71], which combines a user-friendly MATLAB® interface with the computational efficiency of FORTRAN routines [72]. ISOLA performs full waveform inversion by minimizing the least-squares misfit between observed and synthetic seismograms. The quality of fit is quantified using variance reduction (VR), defined as:

$$VR = 1 - \frac{res^2}{data^2} \quad (1)$$

 doi:10.20944/preprints202603.1351.v1

where, res^2represents the sum of squared residuals between observed and synthetic waveforms, $data^2$is the sum of squared amplitudes of the observed data. Higher VR values indicate a better agreement and a well-resolved source solution [71,73].

The preferred solution corresponds to the minimum residual error, thereby maximizing waveform similarity [70,71]. The robustness of the inversion was further evaluated using the condition number (CN), defined as the ratio of the largest to the smallest singular values (or eigenvalues) of the Green's function matrix:

$$CN = \sqrt{\frac{e_{max}}{e_{min}}} \quad (2)$$

where e_{max} and e_{min} denote the maximum and minimum eigenvalues, respectively. A lower CN reflects a well-conditioned and stable inversion [71].

To identify the optimal frequency band for inversion, each waveform component was tested over multiple frequency ranges. The high-frequency cutoff was selected based on epicentral distance and signal quality, whereas the low-frequency limit was constrained by ambient noise levels [74]. Waveforms affected by instrumental noise or malfunction were excluded from the dataset [75,76]. Based on this evaluation, a frequency band of 0.03 Hz–0.05 Hz was selected for the final inversion.

Event locations and moment tensor solutions were computed using the 1-D velocity model proposed by Soomro et al. [77]. Application of this regional velocity structure resulted in a variance reduction of 0.62 and a condition number of 5, indicating a stable and reliable moment tensor solution for the 2019 Mirpur sequence (Table 1, Figures 2 and 3).

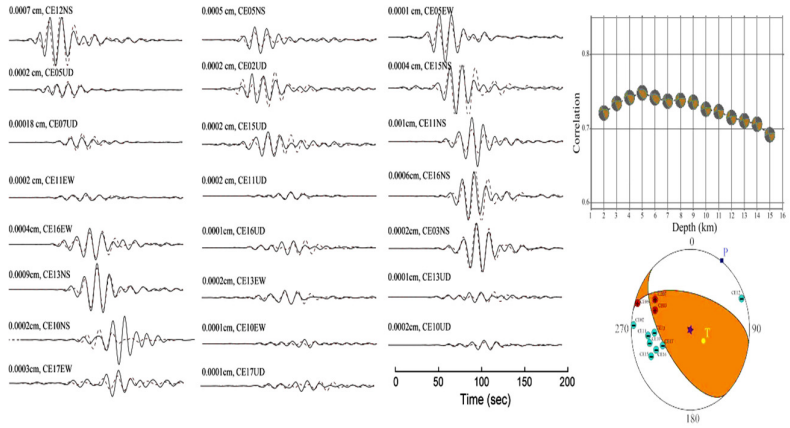

Figure 3. The focal mechanism solution and focal depth of the largest aftershock of the 26 September 2019 Mirpur earthquake (Mw= 4.7) were determined through waveform fitting between observed (solid lines) and synthetic (dotted lines) seismograms. Moment tensor inversion was performed using 23 components recorded at 12 seismic stations. A grid-search method was applied to constrain the focal depth, yielding an optimal depth of 3 km. The model parameters were selected based on the minimum variance reduction criterion.

Table 1. Moment tensor inversion results for the 2019 (M5.8) Mirpur mainshock and its largest aftershock (M4.7). Events time, location, estimated magnitude, and the corresponding focal and nodal planes are shown. Parameters used to assess the quality of the inversion results are also provided.

No	Time yyyymndy hr:min	Location			*Mw*	Plane 1 (Degree)			Plane 2 (Degree)			Vr	CN	DC (%)	CLVD (%)
		Lat.	Long.	Dep. (km)		Str.	Dip	Rake	Str.	Dip	Rake				
1	20190924 11:01	33.06º	73.85º	4.6	5.8	234	13	62	82	79	96	0.62	5.0	99.7	0.3
2	20190926 07:01	33.04º	73.77º	05	4.7	142	48	119	282	49	62	0.56	3.5	98.8	1.2

 doi:10.20944/preprints202603.1351.v1

yyyymndy hr:min: yyyy=year, mn= month, dy= day, hr= hour, min= minute; Lat.= latitude; Long.= longitude; Dept.= depth; Str.=strike; Vr= variance reduction; CN= condition number; DC= double couple; CLVD= compensated linear vector dipole.

3.3. Stress Inversion

The kinematic behavior of the earthquake source area is considered a key element in understanding tectonic processes [78]. Previous studies have proposed several inversion tecniques that utilized focal mechanism solutions as primary input data for estimating the stress tensor [79,80]. Two main assumptions are generally adopted in most stress inversion methods: (1) the stress field is assumed to be homogeneous and unchanged in both space and time, and (2) slip along a fault plane is assumed to occur in the direction of the maximum resolved shear stress [81,82].

Several techniques have been developed to determine the stress field, including the combination of P-wave first-motion polarities with focal mechanism data [83], direct inversion procedures [84], and least-squares grid search methods [85]. In practical applications, four independent parameters, out of the six components of the full stress tensor are sufficient to describe the orientation and relative magnitudes of stresses. These parameters include the three principal stresses: σ1 (maximum compressive stress), σ2 (intermediate compressive stress), and σ3 (minimum compressive stress), ordered such that σ1 ≥ σ2 ≥ σ3 ≥ 0. The fourth parameter is the stress ratio (R), defined as: R=((σ_2-σ_3))/(〖(σ〗_1-σ_3)), where 0 ≤ R ≤ 1.

Accordingly, stress inversion outcomes obtained from these four parameters are constrained by fault-slip measurements and focal mechanism solutions [79,83]. However, a persistent ambiguity exists in identifying the actual fault plane from the two nodal planes provided by a focal mechanism solution [86,87]. To address this uncertainty, several computational tools have been developed; among them, the Win-Tensor program developed by [87] was applied in the present study.

In the initial stage, the dataset was analyzed using the "Right Dihedron" function, which provides preliminary and approximate stress tensor solutions based on focal mechanism solutions (FMS) as input. In some cases, inconsistent or unreliable data were excluded, and only the final stress tensor solutions were retained for subsequent analysis.

The second stage involved "Rotational Optimization," where further refinement of the stress tensor was performed using the Right Dihedron results as input. This procedure applies the F5 composite function, an iterative algorithm designed to reduce the overall misfit, including the potential shear ambiguity between nodal planes. The F5 function is based on two components: one minimizes the misfit angle (α) between the observed slip direction and the modeled slip on a nodal plane, while the other reduces the resolved normal stress to enhance shear stress and decrease friction, thereby promoting slip along the selected fault plane [81].

Importantly, the composite F5 function used in Rotational Optimization is independent of the σ_3/σ_1 ratio and ranges from 0 to 360, where 0 represents a perfect fit and 360 indicates a complete mismatch in the Win-Tensor program.

Within the Right Dihedron approach, both nodal planes, representing compressional and extensional dihedran are treated as equivalent, which constrains the orientation of compressional and extensional stresses. At this stage, no distinction is made between the actual fault plane and the auxiliary plane. However, once a stress tensor is applied, the selected fault plane must correspond to the minimum misfit value, since the fault and auxiliary planes differ in orientation relative to the imposed stress field.

During Rotational Optimization, the stress tensor is evaluated against both nodal planes of each focal mechanism solution to identify the best-fitting configuration. After applying the stress tensor to all focal mechanisms, the nodal plane exhibiting the lower F5 misfit value is interpreted as the likely fault plane. This procedure ensures the selection of the most compatible focal planes and filters the dataset by excluding solutions with an angular misfit greater than 60°. The focal planes with the smallest F5 misfit values are then used to compute an updated stress tensor. This iterative process is repeated until the stress tensor converges to a stable and optimized solution.

 doi:10.20944/preprints202603.1351.v1

Following the determination of the final stress tensors, the tectonic stress regime index (R′) proposed by Delvaux and Sperner [87] was applied to classify the stress environment. In extensional settings, R′ varies between 0 and 1, corresponding to a normal faulting regime. For strike-slip conditions, R′ falls within the range of 1 to 2. In compressional environments, R′ ranges from 2 to 3, indicating a thrust faulting regime.

The orientation and azimuth of the horizontal principal stresses (SHmax and Shmin) were determined using the selected fault planes [88]. These stress orientations were then represented on an equal-area projection. Stress inversion for the Mirpur and Kashmir regions was conducted with Win-Tensor software to assess the current stress conditions. In the Mirpur region, only five focal mechanism solutions were used (Table 2), whereas the Kashmir region included 62 events (Figure 4). The resulting stress inversion showing the SHmax orientation is presented for Mirpur in Figure 5 and for Kashmir in Figure 6.

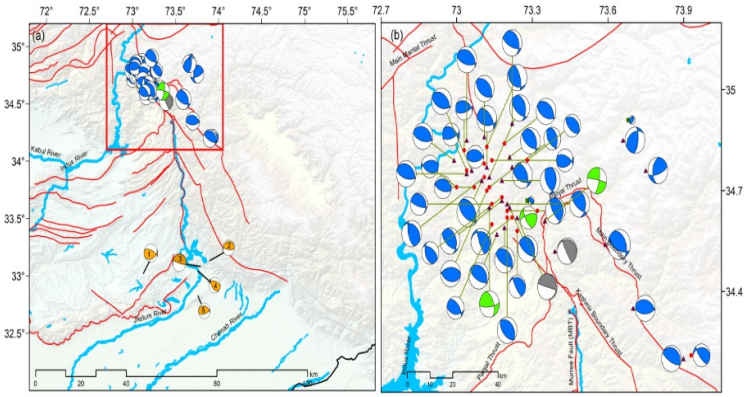

Figure 4. Focal mechanism solutions of the available seismic events for the Mirpur and Kashmir regions that were obtained from the Global CMT catalogue and moment tensor inversion. (a) Beach ball diagrams with corresponding source parameters are listed in Table 2. Events #3 and #4 were derived from moment tensor inversion, whereas Event #5 was taken from [21]. The remaining events were obtained from the Global CMT catalogue. The rectangle outlines the Kashmir region, which is shown in detail in (b). .

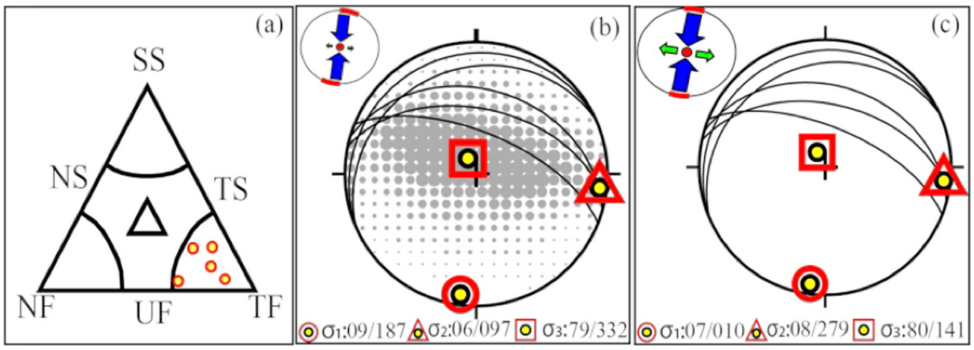

Figure 5. Stress inversion analysis for the Mirpur region was conducted using focal mechanism solutions from five seismic events. The fault planes are illustrated as cyclographic traces on lower-hemisphere, equal-area stereographic projections. The orientations of the principal stress axes—σ1, σ2, and σ3—are indicated by a circle, triangle, and square, respectively. (a) Faulting styles were classified using the Frohlich plot, which shows that all five analyzed events exhibit a purely thrust faulting mechanism. (b) Stereographic projection of the stress inversion results derived using the Right Dihedron method. The relative size of the filled circles represents the density of the compressional quadrants associated with strike-slip events. Dots accompanied by double-headed arrows indicate the resolved shear stress on the selected fault planes, as computed using the Win-Tensor

 doi:10.20944/preprints202603.1351.v1

program. Arrows pointing inward and outward denote the orientations of SHmax and Shmin, respectively (Table 1). (c) Optimized stress inversion results computed using the rotational optimization technique.

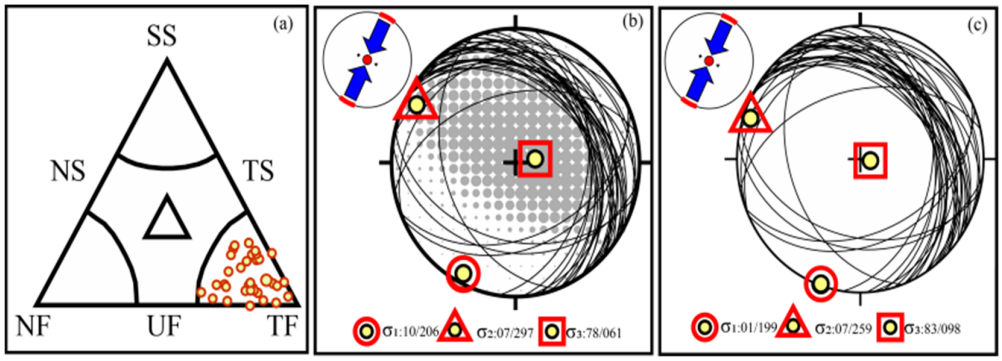

Figure 6. Same as that of Figure 5, but computed for the Kashmir region.

Table 2. Stress inversion results obtained from focal mechanism solutions derived through moment tensor inversion and supplemented by data from the Global CMT catalog for the Mirpur and surrounding region.

No	Time yyyymndy hr:min	Location			*Mw*	Plane 1 (Degree)			Plane 2 (Degree)			Stress inversion			
		Lat.	Long.	Dep. (km)		Str.	Dip	Rake	Str	Dip	Rake	F5	S_{Hmax}	S_{hmin}	R′
1	20010716 07:18	33.01º	73.12º	50.5	5.1	65	36	49	292	64	116	5.6	178	88	2.5
2	20060310 07:50	33.13º	73.89º	10	4.9	246	21	61	96	71	101	2.2	172	82	2.5
3	20190924 11:01	33.06º	73.85º	4.6	5.8	234	13	62	82	79	96	0.5	176	86	2.5
4	20190926 07:01	33.04º	73.77º	05	4.7	142	48	119	282	49	62	0.4	32	122	2.5
5	20241205 06:21	32.80º	73.94º	02	5.0	76	58	72	286	36	116	0.4	172	82	2.5

F5= misfit function; SHmax = Minimum and maximum horizontal stress; Shmin = Minimum horizontal stress.

3.4. Seismogenic Depth

For certain region a delineation of seismogenic activities is characterized by noticeable decrease in background seismicity with depth (varies from 10 km to 20 km across different regions) [89–91]. The thickness of seismogenic layer is generally considered to impact the maximum length of active faults, and consequently the maximum expected magnitude [92,93]. The top depth of basement rock is crucial for controlling the maximum possible potential for the occurrence of major earthquakes [94,95].

Aftershocks of the 2019 Mirpur sequence were used to investigate post-seismic relaxation and estimate the seismogenic depth. Events recorded within 600 days of the mainshock were considered aftershocks, as reported by Tahir et al. [3], are characterized the temporal decay of the sequence using local seismic data and the modified Omori's law.

A dataset comprising 600 events, occurring within 100 km of the mainshock and recorded by a minimum of three seismic stations, was selected for relocation and seismogenic depth estimation. To obtain reliable depth estimates, selection of an appropriate velocity model is essential to minimize artifacts in hypocentral calculations [96]. Seven different velocity models were tested (Figure 7), developed for Pakistan and adjacent regions of India. Three models were developed for Pakistan, referred to as Soomro (published by Soomro et al. [77]), Qaisar (published by Qaisar et al.) [97], and

 doi:10.20944/preprints202603.1351.v1

WinPak (published by Parvez et al. [98]), while India has four models named M01, M02, and M12, each based on distinct datasets, as reported in Parvez et al. [99] (see Figures 3 and 4 for detail). Notably, Soomro et al. [77] provided the only local-scale velocity structure constrained by the same seismic network used in this study, whereas the remaining models were developed at a broader regional scale [77,97,100]. In addition, Soomro et al. [77] proposed a 1-D velocity model for the upper and central Indus Basin of Pakistan using 486 local earthquakes. From the seven tested models, the most suitable velocity structure was identified based on the smallest RMS travel-time residuals (Figure 7). For depth estimation, the horizontal location of each event was fixed and a grid-search approach was applied to determine the optimal depth. The depth corresponding to the minimum RMS value was considered the focal depth of the respective event (Figure 8).

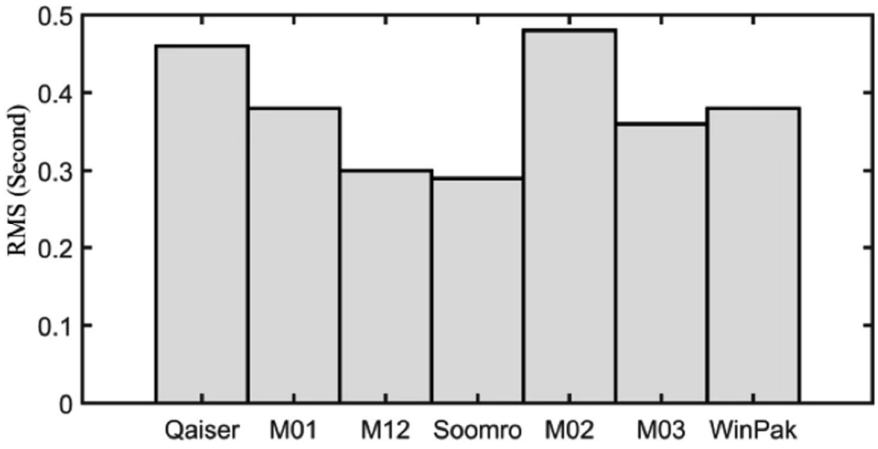

Figure 7. Comparison of RMS (Root Mean Square) travel-time residuals for different velocity models applied in this study for earthquake location. The velocity model yielding the lowest RMS value was selected and subsequently used in the grid-search procedure for estimating focal depths in the seismogenic analysis.

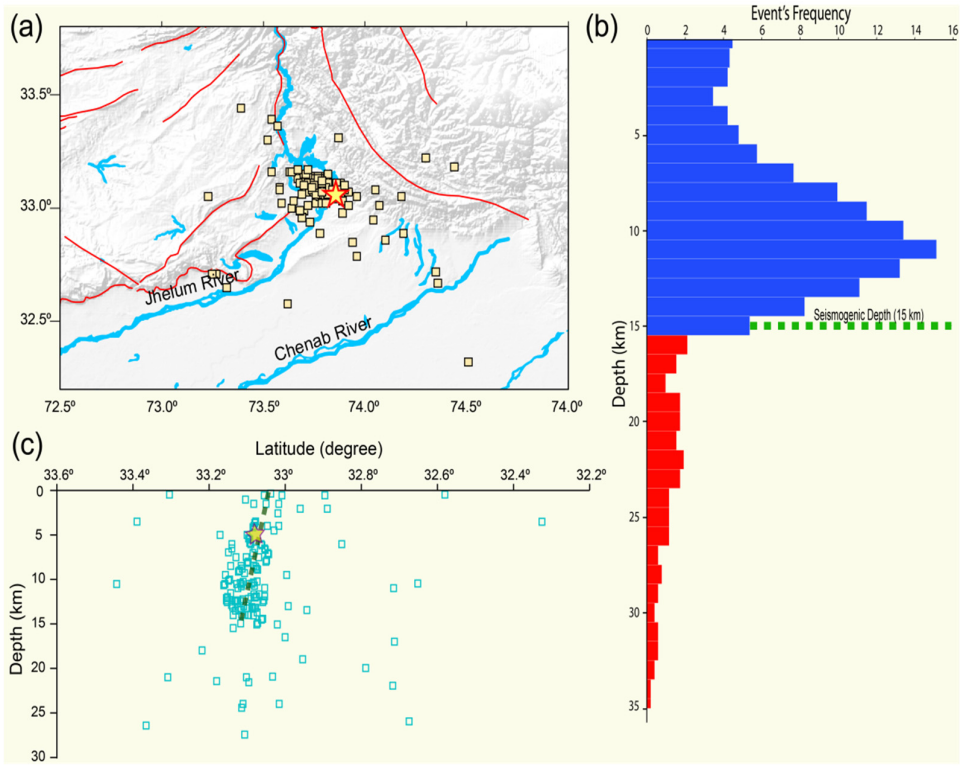

 doi:10.20944/preprints202603.1351.v1

Figure 8. Earthquake relocation and seismogenic depth analysis for the Mirpur region. (a) Spatial distribution of the aftershock sequence determined using the velocity model of [77], which produced the lowest RMS travel-time residuals and was therefore selected for estimating seismogenic depths in this area. (b) Frequency–depth distribution of events obtained through a grid-search approach. For each event, the depth corresponding to the minimum RMS value at a fixed location was adopted as the final focal depth. The seismogenic zone is subdivided into upper and lower layers with a boundary at 15 km depth. Histograms shaded in red represent events shallower than 15 km, whereas blue bars indicate deeper events. The focal depths of the recent earthquakes that occurred in the Mirpur and Kharian areas also fall within the defined seismogenic depth range.

4. Results and Discussion

Moment tensor solutions were determined for the destructive 2019 Mirpur mainshock (Mw= 5.8) and its largest aftershock (Mw= 4.7) using local seismic waveform data to investigate post-seismic relaxation and their relationship with the underlying seismogenic framework. Seismic records from the local networks of the Centre for Earthquake Studies and the Pakistan Meteorological Department were utilized, as these networks provide a lower completeness magnitude compared to other national and international catalogs. The Mirpur earthquake was one of the largest instrumentally recorded event in this area and was located close to the Mangla Dam, highlighting its considerable socio-economic significance (Figure 1). Subsequently, the Kharian earthquake of 12 December 2024 (Mw= 5.0) became the second-largest event in the region following the 2019 sequence.

4.1. Focal Mechanism Solution and Stress Inversion

The focal mechanism solutions for the mainshock (Mw= 5.8) and its largest aftershock (Mw= 4.7) are illustrated in Figures 2 and 3. The robustness of the solutions was assessed using variance reduction (VR) and condition number (CN) values (Table 1), which fall within the acceptable thresholds recommended by [101]. Both events indicate a thrust faulting mechanism with a NW–SE oriented strike, although they differ in dip angle.

The estimated depth of the mainshock (4 km) is comparable to the values reported by [1,2], who suggested depths of 5 km and 6 km, respectively. The low dip angle (10°) is consistent with the solution provided by Global Centroid Moment Tensor. In contrast, United States Geological Survey and [17] reported a relatively higher dip angle (>10°) for this event, whereas [1,2,18], suggested a lower dip angle (<10°). Both low- and high-dip solutions remain plausible, as the earthquake occurred within a fault-propagation fold system (Samwal Fold). A shallow dip angle may indicate linkage with the Main Frontal Thrust (MFT), whereas a steeper dip could reflect slip along a ramp segment of the MFT associated with the regional ramp–anticline structure.

The occurrence of the largest aftershock is significant for understanding both co-seismic stress transfer and post-seismic stress relaxation. The largest aftershock was located slightly south of the mainshock (approximately 20 m) and shows a relatively higher dip angle (40°). This steeper dip suggests the possible activation of a ramp–anticline segment within the thrust fault system.

Moreover, the recent Kharian earthquake, situated approximately 30 km south of this event, has also been associated with fault-propagation fold structures, particularly the Pabbi anticlines, indicating continued tectonic deformation along these compressional features.

The present-day stress inversion was carried out using a total of five focal mechanism solutions (Table 2). Two mechanisms were derived from the moment tensor inversion performed in this study, while three additional solutions were compiled from published literature and the Global Centroid Moment Tensor catalog (Figure 4). The combined dataset was used to determine neotectonics and the direction of the principal stress axes responsible for the seismic sequence.

The derived stress parameters were compared with those reported for the 2005 Kashmir earthquake sequence. The inversion results show that the maximum horizontal compressive stress (SHmax) in the Mirpur region is oriented in a NNE–SSW direction (Figure 5). This orientation closely matches the stress pattern documented for the 2005 Kashmir event and aligns with the overall convergence of the Indian Plate beneath the Eurasian Plate (Figure 6). Such consistency suggests that

 doi:10.20944/preprints202603.1351.v1

the investigated sequence is predominantly controlled by the continued northward motion of the Indian Plate and the associated compressional tectonic regime of the Himalayan foreland.

4.2. Seismogenic Depth

A maximum static Coulomb stress change of 1.3 bar near the epicentral region was reported by [3]. Following the 2019 Mirpur earthquake, the southern and up-dip regions were identified as zones of increased stress. Similarly, [1] suggested a co-seismic stress increase at a depth of ~10 km in the southern segment of the rupture area.

However, the sparse GPS network in this region limits detailed investigation of time-dependent stress evolution and stress triggering associated with the Mirpur earthquake. Therefore, aftershock-based analyses provide an alternative means to understand stress redistribution. In this study, seismogenic depth was estimated using aftershocks recorded up to 600 days after the mainshock. Seven different velocity models (three from Pakistan and four from India) were tested for aftershock relocation. Among these, the local velocity model of [77], developed using the same seismic network data, yielded the lowest travel-time residuals (average variance reduction ~0.2 s). Hence, this model was selected for further analysis, including seismogenic depth estimation (Figure 7).

Using a grid-search approach, the focal depth of each event was determined by minimizing the residual between observed and synthetic travel times. The depth distribution shows a clear peak at ~10 km, which coincides with the level where the Main Himalayan Thrust (MHT) passes through the study area. This suggests post-seismic activation of the MHT. The estimated seismogenic depth is approximately 15 km, indicating that most earthquakes in this region originate within this depth range. Only a few events exceed depths of 17 km (Figure 8), implying that rupture propagation is largely confined to the upper seismogenic layer.

As depth increases, cracks tend to close gradually due to increasing confining pressure, resulting in a more homogeneous stress field in the lower seismogenic layer. Consequently, ruptures initiating at greater depths may propagate more smoothly but can also be temporarily arrested, contributing to aftershock activity [102].

The distribution of event depths with latitude outlines a steeply dipping fault geometry rather than a low-angle structure. These observations suggest that the Mirpur mainshock likely nucleated on the Main Frontal Thrust (MFT) within the seismogenic zone, whereas post-seismic relaxation and aftershock activity occurred along a higher-angle ramp structure, possibly associated with the Samwal fold. This fault-propagation pattern is comparable to the geometry of the Pabbi fold, which also exhibits a relatively high dip angle.

The recent $M > 5.0$ earthquakes in the Mirpur and Kharian region occurred within a structurally complex part of the northwestern Himalayan fold-and-thrust belt. Regional deformation is governed by oblique convergence between the Indian and Eurasian plates, generating a transpressional stress regime [3,21]. In this region, north–south crustal shortening is further complicated by the counterclockwise rotation of the Indian Plate within the Kashmir syntaxis, resulting in strain partitioning, lateral variations in stress orientation, and progressive structural reconfiguration of the frontal orogenic wedge.

The dominant seismogenic structure in the study area is the Main Frontal Thrust (MFT). In Mirpur–Kharian, the MFT is expressed primarily as a blind thrust, with deformation accommodated through fault-propagation folding rather than surface rupture. Surface manifestations include the Samwal Fold near Mirpur and the Pabbi Anticline in the Kharian region, both interpreted as the geomorphic expression of slip along underlying thrust ramps. At depths of approximately 8–10 km, the MFT links downward with the Main Himalayan Thrust (MHT), a regional basal décollement that accommodates underthrusting of the Indian Plate beneath Eurasia. The presence of subsidiary splays and imbricate thrust sheets contributes to mechanical heterogeneity within the wedge, promoting distributed seismic deformation and segmented rupture behavior.

Within this tectonic framework, the 2019 Mirpur mainshock is inferred to have nucleated on a frontal ramp segment of the MFT system. Static stress transfer following the mainshock likely

 doi:10.20944/preprints202603.1351.v1

enhanced Coulomb failure stress on adjacent ramp structures associated with the Samwal and Pabbi folds, facilitating subsequent seismic activity (Figure 9). This pattern is consistent with stress redistribution within an imbricate thrust system, where geometric complexities and ramp–flat transitions localize strain. Furthermore, post-2019 seismic observations suggest a modification of the regional stress field, indicating partial stress reorganization within the frontal Himalayan wedge and its influence on subsequent moderate-magnitude events in the Mirpur–Kharin region [3].

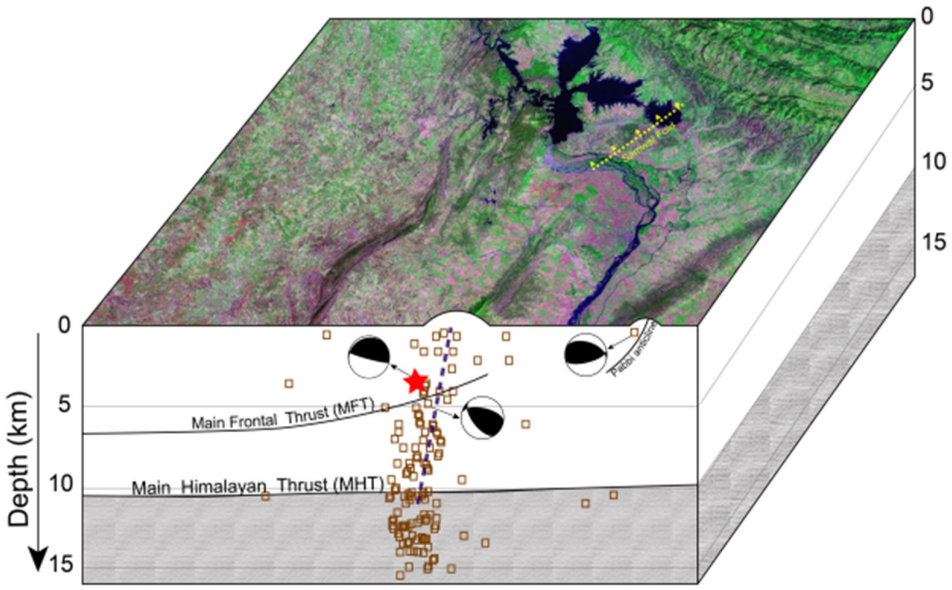

Figure 9. A conceptual model illustrating the association of seismic events with regional and local seismogenic sources. The cross-sectional profile presents the relocated earthquakes together with focal mechanism solutions for the Mirpur mainshock, its largest aftershock, and the Kharian earthquake. Most events occur at depths shallower than 15 km, with a peak concentration around 10 km, corresponding to the interpreted depth of the Main Himalayan Thrust in this region. However, the cross-sectional distribution also delineates a high-angle structure, which may represent a ramp segment of the fault system.

5. Conclusions

Moment tensor inversion of the 2019 Mirpur mainshock and its largest aftershock indicates contrasting fault geometries: the mainshock is characterized by a relatively low-angle thrust consistent with slip along the Main Frontal Thrust (MFT), whereas the largest aftershock exhibits a steeper dip, likely associated with a ramp structure beneath the Samwal Fold. These results highlight the kinematic interaction between frontal thrusts and subsidiary ramp-related structures within the fold-and-thrust belt.

Present-day stress inversion reveals a stress regime comparable to that for the 2005 Kashmir earthquake region, suggesting that deformation is primarily driven by ongoing convergence of the Indian Plate as the first-order tectonics. Relocated aftershocks define a pronounced depth concentration at ~10 km, which corresponds to the level of the Main Himalayan Thrust (MHT), indicating post-seismic activation along the basal décollement. The estimated seismogenic thickness of ~15 km constrains the depth extent of brittle failure in this segment of the northwestern Himalaya.

The Samwal Fold, similar in structural style to the Pabbi fold, represents a seismically active ramp-related blind thrust system. Coulomb stress redistribution following the 2019 Mirpur earthquake likely promoted stress loading on adjacent fault segments, advancing the seismic cycle of nearby structures. The 2024 Pabbi (Kharian) earthquake provides a recent example of such stress interaction within the frontal wedge.

 doi:10.20944/preprints202603.1351.v1

Overall, crustal shortening in the Mirpur–Kharian region appears to be partitioned among major regional thrusts, secondary ramp anticlines, and aseismic slip along a deeper viscous décollement beneath the Salt Range, reflecting a mechanically layered and dynamically evolving orogenic system.

Author Contributions: Conceptualization, M.T.; methodology, M.T., A.A., D.N., K.K. and M.R.; software, M.T., A.A.. R.A., D.N. and C.D.; validation, M.T., G.P., A.A., M.R., D.N., K.K. and M.N.M; formal analysis, M.T., G.P., K.K., C.D., M.R., M.N.M. and A.A.; investigation, M.T., R.A., K.K., M.R., G.P., D.N., C.D., and M.N.M; resources, M.T. and A.A.; data curation, M.T., M.N.M., M.R., D.N., C.D., A.A. and R.A.; writing—original draft preparation, M.T., A.A. and D.N.; writing—review and editing, M.T., R.A., C.D., D.N., M.P., K.K. and T.I.; visualization, M.T. and D.N. ; supervision, T.I.; project administration, T.I.; All authors have read and agreed to the published version of the manuscript.

Funding: This research received no external funding.

Data Availability Statement: Dataset available on request from the authors.

Acknowledgments: The authors are obliged to the officials of CES and the PMD for providing data used in this work. We highly appreciate the support from CES collogues Bilal Saif, Azmat Azad and Muhammad Yousaf Khan. Their valuable suggestion improved figures quality and manuscript's technical writing.

Conflicts of Interest: The authors confirmed that they have no conflict of interest.

References

1. Sreejith, K.; Jasir, M.; Agrawal, R.; Rajawat, A. The 2019 September 24, Mw= 6, Mirpur Earthquake, NW Himalaya: Geodetic Evidence for Shallow, near-Horizontal Décollement Rupture of the Main Himalayan Thrust. *Tectonophysics* **2021**, *816*, 229013.
2. Barkat, A.; Javed, F.; Joe Tan, Y.; Ali, A.; Tahir Javed, M.; Ahmad, N.; Awais, M.; Ali Shah, M.; Iqbal, T. 2019 M w 5.9 Mirpur, Pakistan Earthquake: Insights from Integrating Geodetic, Seismic, and Field Observations. *Seismol. Soc. Am.* **2022**, *93*, 2015–2026.
3. Tahir, M.; Khan, M.Y.; Tahir, S.; Iqbal, T. Crustal Stress Redistribution and Aftershock Patterns in the Northwestern Himalaya Following the 2019 Mirpur Earthquake. *J. Seismol.* **2025**, *29*(6):1615-1635, doi:10.1007/s10950-025-10337-5
4. Khan, M.Y.; Turab, S.A.; Ali, L.; Shah, M.T.; Qadri, S.T.; Latif, K.; Kanli, A.I.; Akhter, M.G. The Dynamic Response of Coseismic Liquefaction-Induced Ruptures Associated with the 2019 M w 5.8 Mirpur, Pakistan, Earthquake Using HVSR Measurements. *Lead. Edge* **2021**, *40*, 590–600.
5. Khan, M.Y.; Turab, S.A.; Riaz, M.S.; Atekwana, E.A.; Muhammad, S.; Butt, N.A.; Abbas, S.M.; Zafar, W.A.; Ohenhen, L.O. Investigation of Coseismic Liquefaction-induced Ground Deformation Associated with the 2019 Mw 5.8 Mirpur, Pakistan, Earthquake Using Near-surface Electrical Resistivity Tomography and Geological *Data. Surf. Geophys.* **2021**, *19*, 169–182.
6. Alam, Z.; Ahmed, S.; Fiaz, M.; Noroozinejad Farsangi, E. An Insight into the Characteristics of the September 24, 2019, MW 5.8 Mirpur, Pakistan, Earthquake and Reconnaissance of the Induced-Failure Modes in Buildings and Civil Infrastructure Facilities. P*ract. Period. Struct. Des. Constr.* **2023**, *28*, 05023005.
7. Habib, W.; Mahmood, S.; Noor, S.; Saleem, A.; Siraj, M.; Ahmad, H. A Post Earthquake Damage Assessment Using GIS in District Mirpur, *Pakistan. Adv. GIS* **2023**, *3*, 53–58.
8. Rafi, M.M.; Ahmed, M.; Lodi, S.H.; Varum, H.; Arshad, M.T. Investigation of Damage to Reinforced Concrete Buildings Due to the 2019 Mirpur Earthquake, Azad Kashmir. *J. Perform. Constr. Facil.* **2022**, *36*, 04022037.
9. Coburn, A.; Spence, R. *Earthquake Protection*; Publisher: John Wiley & Sons, New Jersey, USA, 2002; ISBN 0-470-84923-1.
10. Erdik, M.; Fahjan, Y.; Ozel, O.; Alcik, H.; Mert, A.; Gul, M. Istanbul Earthquake Rapid Response and the Early Warning System. *Bull. Earthq. Eng.* **2003**, *1*, 157–163.
11. Lobo, P.S.; Almeida, J.; Guerreiro, L. Recentring and Control of Peak Displacements of a RC Frame Using Damping Devices. *Soil Dyn. Earthq. Eng.* **2017**, *94*, 66–74.

 doi:10.20944/preprints202603.1351.v1

12. Doocy, S.; Daniels, A.; Packer, C.; Dick, A.; Kirsch, T.D. The Human Impact of Earthquakes: A Historical Review of Events 1980-2009 and Systematic Literature Review. *PLoS Curr.* **2013**, *5*, 67bd14fe457f1db0b5433a8ee20fb833.
13. Cole, M.A.; Elliott, R.J.; Okubo, T.; Strobl, E. Pre-Disaster Planning and Post-Disaster Aid: Examining the Impact of the Great East Japan Earthquake. *Int. J. Disaster Risk Reduct.* **2017**, *21*, 291–302.
14. Kirschenbaum, A.A.; Rapaport, C.; Canetti, D. The Impact of Information Sources on Earthquake Preparedness. *Int. J. Disaster Risk Reduct.* **2017**, *21*, 99–109.
15. Davis, C.; Keilis-Borok, V.; Molchan, G.; Shebalin, P.; Lahr, P.; Plumb, C. Earthquake Prediction and Disaster Preparedness: Interactive Analysis. *Nat. Hazards Rev.* **2010**, *11*, 173–184.
16. Ren, P.; Xu, Z.; Gu, J. Assessments of the Effectiveness of an Earthquake Emergency Plan Implementation with Hesitant Analytic Hierarchy Process. *Int. J. Inf. Technol. Decis. Mak.* **2016**, *15*, 1367–1389.
17. Vaka, D.S.; Rao, Y.S.; Singh, T. Surface Deformation of the 2019 Mirpur Earthquake Estimated from Sentinel-1 InSAR Data. In Proceedings of the 2020 IEEE India Geoscience and Remote Sensing Symposium (InGARSS); IEEE, 2020; pp. 130–133.
18. Tan, Y.; Dai, Z.; Liu, B.; Zha, X. Source Parameters and Slip Distribution of the 2019 M w 5.8 Mirpur (Pakistan) Earthquake Inferred from the Corrected InSAR Observations. *Seismol. Soc. Am.* **2022**, *93*, 1464–1478.
19. Gardezi, S.A.H.; Hussain, G.; Neupane, B.; Imran, M.; Hamid, Q.Y.; Ikram, N.; Usmani, N.A.; Asghar, H. Geological Investigation of 5.6 MW Mirpur Earthquake, Northwestern Himalayas, Pakistan. *Int. Res. J. Earth Sci.* **2021**, *9*, 20–31.
20. Yin, A. Cenozoic Tectonic Evolution of the Himalayan Orogen as Constrained by Along-Strike Variation of Structural Geometry, Exhumation History, and Foreland Sedimentation. *Earth-Sci. Rev.* **2006**, *76*, 1–131.
21. Tahir, M.; Saif, B.; Habib, R.A.; Javed, F.; Iqbal, M.Z.; Iqbal, T.; Mahmood, N.; Ahmed, N. Seismotectonic Analysis of Pabbi Blind-Thrust in the NW Himalayan Foreland: Evidence from the 2024 Kharian Earthquake: *Pure Appl. Geophys.* **2026**, 1–16. https://doi.org/10.1007/s00024-026-03929-w
22. Safi, I.; Rehman, G.; Yaseen, M.; Wahid, S.; Nouman, M.; Fida, S.; Gul, S.; Anjum, M.N. Effects of Transpression on the Rocks Exposed at the Jhelum Fault Zone in the East of Potwar Basin, Pakistan: Implications on the Subsurface Deformation Pattern. *J. Pet. Explor. Prod. Technol.* **2021**, *11*, 2407–2424, doi:10.1007/s13202-021-01224-z.
23. McCaffrey, R.; Nabelek, J. Role of Oblique Convergence in the Active Deformation of the Himalayas and Southern Tibet Plateau. *Geology* **1998**, *26*, 691–694.
24. Avouac, J.-P.; Bollinger, L.; Lavé, J.; Cattin, R.; Flouzat, M. Le Cycle Sismique En Himalaya. *Comptes Rendus Académie Sci.-Ser. IIA-Earth Planet. Sci.* **2001**, *333*, 513–529.
25. Khan, M.A.; Bendick, R.; Bhat, M.I.; Bilham, R.; Kakar, D.M.; Khan, S.F.; Lodi, S.H.; Qazi, M.S.; Singh, B.; Szeliga, W. Preliminary Geodetic Constraints on Plate Boundary Deformation on the Western Edge of the Indian Plate from TriGGnet (Tri-University GPS Geodesy Network). *J .Himal. Earth Sci.* **2008**, *41*, 71–87.
26. Szeliga, W.; Bilham, R.; Kakar, D.M.; Lodi, S.H. Interseismic Strain Accumulation along the Western Boundary of the Indian Subcontinent. *J. Geophys. Res.* **2012**, *117*, B08404, doi:10.1029/2011JB008822.
27. Szeliga W, Historical and modern seismotectonics of the Indian plate with an emphasis on its western boundary with the Eurasian plate, Ph.D. Thesis, College of Information Sciences and Technology, Pennsylvania State University, United States, 2010.
28. Kundu, B.; Yadav, R.K.; Bali, B.S.; Chowdhury, S.; Gahalaut, V.K. Oblique Convergence and Slip Partitioning in the NW Himalaya: Implications from GPS Measurements. *Tectonics* **2014**, *33*, 2013–2024.
29. Avouac, J.-P.; Ayoub, F.; Wei, S.; Ampuero, J.-P.; Meng, L.; Leprince, S.; Jolivet, R.; Duputel, Z.; Helmberger, D. The 2013, Mw 7.7 Balochistan Earthquake, Energetic Strike-Slip Reactivation of a Thrust Fault. *Earth Planet. Sci. Lett.* **2014**, *391*, 128–134.
30. Shaukat, A.Z.; Tahir, M.; Iqbal, T.; Iqbal, T.; Shah, M.A. Seismotectonic Analysis of the 7 October 2021 M w 5.9 Harnai Earthquake, Pakistan. *Bull Seism. Soc. Am.* **2023**, *113*, 636–647.
31. Shaukat, A.Z.; Tahir, M.; Iqbal, T.; Iqbal, T.; Shah, M.A. Seismic Interactions Between Northern Terminus of Ornahc-Nal and Hoshab Faults Based on Source Mechanism Investigation of 06 May 2022 Mw 5.4 Khuzdar Earthquake. *Pure Appl. Geophys.* **2023**, *180*, 3435–3455, doi:10.1007/s00024-023-03352-5.

 doi:10.20944/preprints202603.1351.v1

32. Tahir, M.; Grasso, J.R. Aftershock Patterns of M S> 7 Earthquakes in the India–Asia Collision Belt: Anomalous Results from the Muzaffarabad Earthquake Sequence, Kashmir, 2005. *Bull Seism. Soc. Am.* **2014**,*104*, 1–23.
33. Mukherjee, S. A Review on Out-of-Sequence Deformation in the Himalaya. *Geol. Soc. Lond. Spec. Publ.* **2015**, *412*,109 - 167, https://doi.org/10.1144/sp412.13.
34. Quittmeyer, R.C.; Farah, A.;Jacob, K.H. The seismicity of Pakistan and Its Relation to Surface Faults. In: Geodynamics of Pakistan, Farah, A.; DeJong, K. A. Eds; Lamont-Doherty Geological Observatory Contribution, No. 2667, Geological Survey of Pakistan, Quetta, 1979; pp. 271-284.
35. Davis, D.; Suppe, J.; Dahlen, F. Mechanics of Fold-and-Thrust Belts and Accretionary Wedges. J. *Geophys. Res. B Solid Earth* **1983**, *88*, 1153–1172.
36. Davis, D.M.; Engelder, T. The Role of Salt in Fold-and-Thrust Belts. *Tectonophysics* **1985**, *119*, 67–88.
37. Jaumé, S.C.; Lillie, R.J. Mechanics of the Salt Range-Potwar Plateau, Pakistan: A Fold-and-Thrust Belt Underlain by Evaporites. *Tectonic*s **1988**, *7*, 57–71.
38. Bilham, R.; Bendick, R.; Wallace, K. Flexure of the Indian Plate and Intraplate Earthquakes. *J. Earth Syst. Sci.* **2003**, *112*, 315–329.
39. Bilham, R.; Lodi, S.; Hough, S.; Bukhary, S.; Khan, A.M.; Rafeeqi, S.F.A. Seismic Hazard in Karachi, Pakistan: Uncertain Past, Uncertain Future. *Seism. Res. Lett.* **2007**, *78*, 601–613.
40. Thakur, V.C. Active Tectonics of Himalayan Frontal Fault System. *Int. J. Earth Sci.* **2013**, *102*, 1791–1810.
41. Yeats, R.S.; Lillie, R.J. Contemporary Tectonics of the Himalayan Frontal Fault System: Folds, Blind Thrusts and the 1905 Kangra Earthquake. *J. Struct. Geol*. **1991**, *13*, 215–225.
42. Yeats, R.S.; Thakur, V.C. Active Faulting South of the Himalayan Front: Establishing a New Plate Boundary. *Tectonophysics* **2008**, *453*, 63–73.
43. Searle, M.P.; Treloar, P.J. *Introduction to Himalayan Tectonics: A Modern Synthesis,* The Geological Society of London, UK, 2019, Vol. 483, pp. 1–17, ISBN 0305-8719.
44. Lavé, J.; Avouac, J.-P. Active Folding of Fluvial Terraces across the Siwaliks Hills, Himalayas of Central Nepal. *J. Geophys. Res. Solid Earth* **2000**, *105*, 5735–5770.
45. Le Roux-Mallouf, R.; Godard, V.; Cattin, R.; Ferry, M.; Gyeltshen, J.; Ritz, J.-F.; Drupka, D.; Guillou, V.; Arnold, M.; Aumaître, G. Evidence for a Wide and Gently Dipping Main Himalayan Thrust in Western Bhutan. *Geophys. Res. Lett.* **2015**, *42*, 3257–3265.
46. Vassallo, R.; Mugnier, J.-L.; Vignon, V.; Malik, M.A.; Jayangondaperumal, R.; Srivastava, P.; Jouanne, F.; Carcaillet, J. Distribution of the Late-Quaternary Deformation in Northwestern Himalaya. *Earth Planet. Sci. Lett.* **2015**, *411*, 241–252.
47. Wellman, H. Active Wrench Faults of Iran, Afghanistan and Pakistan. *Geol. Rundsch.* **1966**, *55*, 716–735.
48. Lawrence, R.D.; Yeats, R.S.; Khan, S.H.; Farah, A.; DeJong, K.A. Thrust and Strike Slip Fault Interaction along the Chaman Transform Zone, Pakistan. *Geol. Soc. Lond. Spec. Publ.* **1981**, *9*, 363–370.
49. 4Lawrence, R.D.; Hasan Khan, S.; Nakata, T. Chaman Fault, Pakistan-Afghanistan. *Ann. Tectonicae* **1992**, *6*, 196–223.
50. Farah, A.; Abbas, G.; De Jong, K.A.; Lawrence, R.D. Evolution of the Lithosphere in Pakistan. *Tectonophysics* **1984**, *105*, 207–227.
51. Haq, S.S.; Davis, D.M. Oblique Convergence and the Lobate Mountain Belts of Western Pakistan. *Geology* **1997**, *25*, 23–26.
52. Jadoon, I.A.; Ding, L.; Jadoon, S.-R.K.; Bhatti, Z.I.; Shah, S.T.; Qasim, M. Lithospheric Deformation and Active Tectonics of the NW Himalayas, Hindukush, and Tibet. *Lithosphere* **2021**, 7866954.
53. Mugnier, J.-L.; Gajurel, A.; Huyghe, P.; Jayangondaperumal, R.; Jouanne, F.; Upreti, B. Structural Interpretation of the Great Earthquakes of the Last Millennium in the Central Himalaya. *Earth-Sci. Rev.* **2013**, *127*, 30–47.
54. Grandin, R.; Vallée, M.; Satriano, C.; Lacassin, R.; Klinger, Y.; Simoes, M.; Bollinger, L. Rupture Process of the Mw= 7.9 2015 Gorkha Earthquake (Nepal): Insights into Himalayan Megathrust Segmentation. *Geophys. Res. Lett.* **2015**, *42*, 8373–8382.

 doi:10.20944/preprints202603.1351.v1

55. Jouanne, F.; Gajurel, A.; Mugnier, J.-L.; Bollinger, L.; Adhikari, L.B.; Koirala, B.; Cotte, N.; Bhattarai, R.; Pecher, A.; Bascou, P. Postseismic Deformation Following the April 25, 2015 Gorkha Earthquake (Nepal): Afterslip versus Viscous Relaxation. *J. Asian Earth Sci.* **2019**, *176*, 105–119.
56. Davis, D.M.; Lillie, R.J. Changing Mechanical Response during Continental Collision: Active Examples from the Foreland Thrust Belts of Pakistan. *J. Struct. Geol.* **1994**, *16*, 21–34.
57. Jouanne, F.; Awan, A.; Madji, A.; Pêcher, A.; Latif, M.; Kausar, A.; Mugnier, J.L.; Khan, I.; Khan, N.A. Postseismic Deformation in Pakistan after the 8 October 2005 Earthquake: Evidence of Afterslip along a Flat North of the Balakot-Bagh Thrust. *J. Geophys. Res.* **2011**, *116*, B07401, doi:10.1029/2010JB007903.
58. Jouanne, F.; Awan, A.; Pêcher, A.; Kausar, A.; Mugnier, J.; Khan, I.; Khan, N.; Van Melle, J. Present-day Deformation of Northern Pakistan from Salt Ranges to Karakorum Ranges. *J. Geophys. Res. Solid Earth* **2014,** *119*, 2487–2503.
59. Jouanne, F.; Munawar, N.; Mugnier, J.; Ahmed, A.; Awan, A.A.; Bascou, P.; Vassallo, R. Seismic Coupling Quantified on Inferred Décollements beneath the Western Syntaxis of the Himalaya. *Tectonics* **2020**, *39*, e2020TC006122.
60. Meyer, P.; Jouanne, F.; Doin, M.-P.; Ahmed, A.; Awan, A.A.; Mugnier, J.L. Present-Day Quantification of Seismic Coupling along the Décollement Level beneath the Potwar Plateau Region in Pakistan Western Himalaya. *Earth Planet. Sci. Lett.* **2024**, *637*, 118723.
61. Shah, A.A.; Sahari, S.; Navakanesh, B.; Nurhafizah, A.M.; Fui, F.; Ashwini, T.Q. Tectonic Geomorphology of the Jhelum Fault Zone and Its Contiguous Regions in Western Himalaya. *Bulletin of the Geological Society of Malaysia*, **2022**, *73*, 119-138. https://doi.org/10.7186/bgsm73202210.
62. Tahir, M.; Saif, B.; Iqbal, T.M.; Habib, R.A.; Iqbal, T.; Awais, M.; Shah, M.A. Probing the Active Kinematics in Northwestern Himalayan Foreland, Pakistan: Insights from Seismicity and Gravity Data. *J. Geodyn.* **2025**, *164*, 102100.
63. Lienert, B.R.; Havskov, J. A. Computer Program for Locating Earthquakes Both Locally and Globally. *Seism. Res Lett.* **1995**, *66*, 26–36.
64. Lienert, B.R.; Berg, E.; Frazer, L.N. Hyphocenter: An Earthquake Location Method Using Centered, Scaled, and Adaptively Damped Least Squares. *Bull Seism. Soc. Am.* **1986**, *76*, 771–783.
65. Havskov, J.; Voss, P.H.; Ottemöller, L. Seismological Observatory Software: 30 Yr of SEISAN. *Seism. Res. Lett.* **2020**, *91*, 1846–1852.
66. Ottemöller, L.; Voss, P.; Havskov, J. Seisan Earthquake Analysis Software for Windows, Solaris, Linux and MacOsX. Department Earth Science, University Bergen, Bergen, Norway, 2011, 1-335.
67. Mushtaq, M.; Tahir, M.; Iqbal, M.; Shah, M.; Iqbal, S. Calibration of Local Magnitude Scale for Hindukush Continental Subduction Zone. *Earthq. Sci.* **2021**, *34*, 114–122.
68. Mushtaq, M.N.; Tahir, M.; Shah, M.A.; Khanam, F. Development of Local Magnitude Scale for the Northern Punjab, Pakistan. *J Seism.* **2019**, *23*, 403–416.
69. Tahir, M.; Khan, A.; Mushtaq, M.N.; Iqbal, M.T.; Iqbal, T.; Shah, M.A.; Khan, K.; Soomro, R.A. Distance Attenuation and Local Magnitude Scale Based on Constant Geometrical Spreading in Northern Punjab, Pakistan. *Acta Geophys.* **2021**, *69*, 1567–1584.
70. Sokos, E.N.; Zahradnik, J. ISOLA a Fortran Code and a Matlab GUI to Perform Multiple-Point Source Inversion of Seismic Data. *Comput. Geosci.* **2008**, *34*, 967–977.
71. Zahradník, J.; Sokos, E. ISOLA Code for Multiple-Point Source Modeling. In *Moment Tensor Solutions*, S. D'Amico Ed.; Springer, Springer International Publishing AG, 2019, pp. 1–28, https://doi.org/10.1007/978-3-319-77359-9_1.
72. Triantafyllis, N.; Venetis, I.E.; Fountoulakis, I.; Pikoulis, E.-V.; Sokos, E.; Evangelidis, C.P. Gisola: A High-Performance Computing Application for Real-Time Moment Tensor Inversion. *Seismol. Soc. Am.* **2022**, ^, 957–966.
73. Sabahat, S.; Tahir, M.; Munir, F.; Saif, B.; Iqbal, M.T.; Iqbal, J.; Iqbal, T. Inversion Techniques for Focal Mechanism Determination of Small-Magnitude Earthquakes: A Comparative Study Using the Burewala Earthquake (M W~ 4) in Pakistan. *J. Seismol.* **2024**, *28*, 119–131.
74. Sabahat, S.; Tahir, M.; Iqbal, M.T.; Iqbal, J.; Iqbal, T. Source Parameters of the Fatehjang, Pakistan Earthquake Mw 4.1 of 28 August 2020. *Arab J. Geosci.* **2022**, *15*, 1–17.

 doi:10.20944/preprints202603.1351.v1

75. Zahradník, J.; Plesinger, A. Long-Period Pulses in Broadband Records of near Earthquakes. *Bull. Seismol. Soc. Am.* **2005**, *95*, 1928–1939.
76. Zahradník, J.; Custódio, S. Moment Tensor Resolvability: Application to Southwest Iberia. *Bull. Seismol. Soc. Am.* **2012**, *102*, 1235–1254.
77. Soomro, R.A.; Iqbal, S.; Shah, M.A.; Iqbal, T. P-Wave Minimum 1D Velocity Model for Central and Northern Pakistan. *J .Seismol.* **2022**, *26*, 1039–1049.
78. 7Mai, P.M.; Schorlemmer, D.; Page, M.; Ampuero, J.-P.; Asano, K.; Causse, M.; Custodio, S.; Fan, W.; Festa, G.; Galis, M. The Earthquake-Source Inversion Validation (SIV) Project. *Seismol. Res. Lett.* **2016**, *87*, 690–708.
79. Gephart, J.W. Stress and the Direction of Slip on Fault Planes. *Tectonics 1990*, **9**, 845–858.
80. Hardebeck, J.L.; Hauksson, E. Crustal Stress Field in Southern California and Its Implications for Fault Mechanics. *J. Geophys. Res. Solid Earth* **2001**, *106*, 21859–21882.
81. Delvaux, D.; Barth, A. African Stress Pattern from Formal Inversion of Focal Mechanism Data. *Tectonophysics* **2010,** *482*, 105–128.
82. Lisle, R.J. A Critical Look at the Wallace-Bott Hypothesis in Fault-Slip Analysis. *Bull. Société Géologique Fr.* **2013**, *184*, 299–306.
83. Angelier, J. Inversion of Field Data in Fault Tectonics to Obtain the Regional Stress—III. A New Rapid Direct Inversion Method by Analytical Means. *Geophys. J. Int.* **1990**, *103*, 363–376.
84. Reches, Z. Determination of the Tectonic Stress Tensor from Slip along Faults That Obey the Coulomb Yield Condition. *Tectonics* **1987**, *6*, 849–861.
85. Angelier, J.; Tarantola, A.; Valette, B.; Manoussis, S. Inversion of Field Data in Fault Tectonics to Obtain the Regional Stress—I. Single Phase Fault Populations: A New Method of Computing the Stress Tensor. *Geophys J. Int.* **1982**, *69*, 607–621.
86. Carey-Gailhardis, E.; Mercier, J.L. A Numerical Method for Determining the State of Stress Using Focal Mechanisms of Earthquake Populations: Application to Tibetan Teleseisms and Microseismicity of Southern Peru. *Earth Planet. Sci. Lett.* **1987**, *82*, 165–179.
87. Delvaux, D.; Sperner, B. New Aspects of Tectonic Stress Inversion with Reference to the TENSOR Program. *Geol. Soc. Lond. Spec. Publ.* **2003**, *212*, 75–100.
88. Lund, B.; Townend, J. Calculating Horizontal Stress Orientations with Full or Partial Knowledge of the Tectonic Stress Tensor. *Geophys J. Int.* **2007**, *170*, 1328–1335.
89. Chiarabba, C.; Jovane, L.; DiStefano, R. A New View of Italian Seismicity Using 20 Years of Instrumental Recordings. *Tectonophysics* **2005**, *395*, 251–268.
90. Chung, T.W.; Iqbal, M.Z.; Lee, Y.; Yoshimoto, K.; Jeong, J. Depth-Dependent Seismicity and Crustal Heterogeneity in South Korea. *Tectonophysics* **2018,** *749*, 12–20.
91. Iqbal, M.Z.; Chung, T.W.; Zhou, H.; Cho, S.O.; Nam, M.J. Seismicity Boundary Depth of Mainland China. *Ann. Geophys.* **2018**, *61*(4),SE445. https://doi.org/10.4401/ag-7699.
92. Jackson, J.A.; White, N.J. Normal Faulting in the Upper Continental Crust: Observations from Regions of Active Extension. *J. Struct. Geol.* **1989**, *11*, 15–36.
93. Wells, D.L.; Coppersmith, K.J. New Empirical Relationships among Magnitude, Rupture Length, Rupture Width, Rupture Area, and Surface Displacement. *Bull. Seismol. Soc. Am.* **1994**, *84*, 974–1002.
94. Jackson, J.; Fitch, T. Basement Faulting and the Focal Depths of the Larger Earthquakes in the Zagros Mountains (Iran). *Geophys. J. Int.* **1981**, *64*, 561–586.
95. Avouac, J.-P.; Schubert, G. Mountain Building: From Earthquakes to Geological Deformation. Dynamical Processes, Extensional Compressional Settings. In *Treatise on Geophysics*, Publisher: Elsevier, 2007, 6, pp.377–439.
96. Kissling, E.; Kradolfer, U.; Maurer, H. *Program VELEST User's Guide-Short Introduction.* Institute of Geophysics and Swiss Seismological Service, ETH: Zurich, Switzerland, 1995, 26p.
97. Qaisar, M.; Shahid, M.B.; Mahmood, T.; Khan, K.; Ahmad, S. Velocity Structure and Hypocentral Location of Earthquakes by Simultaneous Inversion Method: Application to the Area of Kalabagh, Pakistan. *J. Himal. Earth Sci.* **2014**, *47*, 141–149.

 doi:10.20944/preprints202603.1351.v1

98. Reiter, D.; Rodi, W.; Johnson, M. Development of a Tomographic Upper-Mantle Velocity Model beneath Pakistan and Northern India for Improved Regional Seismic-Event Location. *Bull. Seismol. Soc. Am.* **2005**, *95*, 926–940.
99. Parvez, I.A.; Vaccari, F.; Panza, G.F. A Deterministic Seismic Hazard Map of India and Adjacent Areas. *Geophys. J. Int.* **2003**, *155*, 489–508.
100. Johnson, M.; Vincent, C. Development and Testing of a 3D Velocity Model for Improved Event Location: A Case Study for the India-Pakistan Region. *Bull. Seism. Soc. Am.* **2002**, *92*, 2893–2910.
101. Sokos, E.; Zahradník, J. Evaluating Centroid-moment-tensor Uncertainty in the New Version of ISOLA Software. *Seismol. Res. Lett.* **2013**, *84*, 656–665.
102. Mori, J.; Abercrombie, R.E. Depth Dependence of Earthquake Frequency-magnitude Distributions in California: Implications for Rupture Initiation. *J. Geophys. Res. Solid Earth* **1997**, *102*, 15081–15090.
103. Yeats, R.S.; Lillie, R.J. Contemporary Tectonics of the Himalayan Frontal Fault System: Folds, Blind Thrusts and the 1905 Kangra Earthquake. *J. Struct. Geol.* **1991**, *13*, 215–225.
104. Blisniuk, P.M.; Sonder, L.J.; Lillie, R.J. Foreland Normal Fault Control on Northwest Himalayan Thrust Front Development. *Tectonics* **1998**, *17*, 766–779, doi:10.1029/98TC01870.
105. DiPietro, J.A.; Pogue, K.R. Tectonostratigraphic Subdivisions of the Himalaya: A View from the West. *Tectonics* **2004**, *23*(5), TC5001, https://doi.org/10.1029/2003TC001554.